Materials Characterization 159 (2020) 110036

Contents lists available at ScienceDirect

Materials Characterization

journal homepage: www.elsevier.com/locate/matchar

Solar-driven photocatalytic removal of organic pollutants over direct Z-scheme coral-branch shape Bi_2O_3/SnO_2 composites

Liangliang Chu[a,b], Jing Zhang[c], Zisheng Wu[a], Chen Wang[a], Yuanyuan Sun[a], Shuying Dong[a,*], Jianhui Sun[a,*]

[a] Key Laboratory for Yellow River and Huai River Water Environmental and Pollution Control, Ministry of Education, Henan Key Laboratory for Environmental Pollution Control, School of Environment, Henan Normal University, Xinxiang, Henan 453007, PR China
[b] Xinxiang University, Xinxiang, Henan 453007, PR China
[c] Sanmenxia Polytechnic, Sanmenxia, Henan 472000, PR China

ARTICLE INFO

Keywords:
Bismuth oxide
Stannic oxide
Z-scheme
Photocatalysis
Organic pollutant

ABSTRACT

Here, we report a feasible strategy to construct a Z-scheme Bi_2O_3/SnO_2 composite via a facile hydrothermal method. Photocatalytic activity of the as-prepared photocatalysts was evaluated through photocatalytic degradation of bisphenol A (BPA) under simulated sunlight irradiation. A photocatalytic efficiency of 93.42% was achieved by $1Bi_2O_3/SnO_2$ during 60 min of irradiation, which was 14.97- and 2.54-fold greater than the photocatalytic efficiency of pure SnO_2 and Bi_2O_3, respectively. In addition, the composite was effective in the photocatalytic decomposition of several antibiotics. Degradation conditions, such as the catalyst dosage, the initial concentration, and pH of BPA aqueous solution, were also investigated. The enhanced photocatalytic degradation efficiency of Bi_2O_3/SnO_2 composites was attributable to the increased absorption of light, as well as the effective separation of photo-induced carriers that resulted from the formation of a Z-scheme heterojunction. The main active species in photocatalytic degradation of BPA by Bi_2O_3/SnO_2 composite were h^+ and $^1O_2$. This highly efficient and broad-spectrum photocatalyst renders it a promising candidate for water pollution control.

1. Introduction

Nowadays, large-scale development of industry brings serious pollution to the environment. A large quantity of untreated and contaminated discharge containing various organic and inorganic substances is releasing into environment, which has caused widespread concern [1]. Among, bisphenol A (BPA) is an organic pollutant that is mainly used to produce various polymer materials, including the epoxy resins and polycarbonate plastics, and can also be used to manufacture fine chemical products such as plasticizers. However, BPA is an endocrine disruptor and its presence in the environment may threaten human health, including sexual precocity, embryotoxicity, and teratogenicity. Moreover, BPA is non-biodegradable and is even difficult to degrade chemically [2]. Therefore, convenient and efficient techniques to eliminate BPA from the environment are required.

Until now, various methods such as adsorption [3], chemical remediation [4] and multiple advanced oxidation [5] including Fenton oxidation [6], H_2O_2 oxidation [7], photocatalytic degradation [8], and persulfate (PS) activation have been studied to eliminate BPA. Among them, photocatalysis is thought to have more potential due to its efficiency, environmental friendliness and safety. Over the past few decades, various photocatalytic materials have been developed to remove pollutants from wastewater, such as $BiVO_4$ [9], $ZnSn(OH)_6$ [10], ZnO [11], g-C_3N_4 [12,13], TiO_2 [14,15], SnO_2 [16], MoS_2 [17] etc. SnO_2 is a promising photocatalyst due to its physical and chemical stability, abundance and non-toxicity. Nevertheless, the large band gap energy (E_g) of SnO_2 (3.56–3.66 eV) [18], as well as high recombination possibility of photogenerated carriers, result in poor photocatalytic activity and hence restrict its practical application. In order to solve this issue, different strategies have been developed, encompassing element doping [19], heterojunction fabrication [20], deposition of noble metals [21], morphology control [22], etc. Hybridization with narrow bandgap semiconductors, such as SnO_2/BiOBr [18], ZnO/SnO_2 [23], and SnO_2/g-C_3N_4 [24], is an effective way to improve the photocatalytic performance of SnO_2.

Along this line, Bi_2O_3, with a relative narrow bandgap energy of 2.8 eV and matched band position with SnO_2, was selected to couple with SnO_2 aiming to realize augmented photocatalytic property. For instance, Sun et al. [25] found that SnO_2/Bi_2O_3 enhanced the degradation rate of 2,4-DCP by 23% compared with Bi_2O_3. Qiu et al. [26]

* Corresponding authors.
E-mail addresses: dongsy@htu.edu.cn (S. Dong), sunjhhj@163.com (J. Sun).

https://doi.org/10.1016/j.matchar.2019.110036
Received 31 July 2019; Received in revised form 4 November 2019; Accepted 25 November 2019
Available online 29 November 2019
1044-5803/

reported that 98.1% of RhB. can be completely decolorized by a SnO_2/Bi_2O_3 composite within 30 min under 400 W halide metal lamp irradiation. However, present researches about SnO_2/Bi_2O_3 composites exist several issues. First, some preparation processes involve many steps, which are rather troublesome. Second, the solid-state synthesis strategy needs high temperature, which brings about high energy cost. Third, the improvement of photocatalytic performances is not significant. Thereby, to fabricate SnO_2/Bi_2O_3 composites with tailorable morphologies and favorable photocatalytic activities by a simple and cost-effective method is of great significance.

Herein, we develop a facile in-situ hydrothermal method to couple Bi_2O_3 coral branches with hollow SnO_2 to fabricate direct Z-scheme Bi_2O_3/SnO_2 composite. Various characterization techniques, including ultraviolet-visible diffuse reflectance (UV–vis DRS) spectroscopy, photoluminescence spectroscopy (PL), and electron spin resonance (ESR), were used to investigate the prepared samples in detail. Accordingly, a direct Z-scheme photocatalytic mechanism is proposed based on the ESR result and the relative band positions of bare Bi_2O_3 and SnO_2.

2. Experimental procedure

2.1. Preparation of materials

All reagents were of analytical grade and used as received without further purification. Deionized water was used during the experimental process. The composite Bi_2O_3/SnO_2 samples were prepared as follows: a certain amount of bismuth nitrate pentahydrate ($Bi(NO_3)_3{\cdot}5H_2O$) (> 99.0%) was dissolved into 30 mL mixed solution of absolute ethanol (vol% = 25%) and deionized water under magnetic stirring for 30 min. Then, 2 mmol sodium stannate ($Na_2SnO_3{\cdot}3H_2O$; > 99.0%) was added to the solution and continuously stirred for another 30 min. The reaction solution was then transferred to a 50 mL stainless steel Teflon-lined autoclave and kept at 180 °C for 24 h. After cooling down, the product was collected by centrifugation, washed separately with absolute ethanol and water each for three times, and dried in an oven at 60 °C overnight. The final product xBi_2O_3/SnO_2 composite was obtained after calcination at 450 °C for 2 h in a muffle furnace, where x is the molar ratio of Bi_2O_3 to SnO_2. With varying the amounts of $Bi(NO_3)_3{\cdot}5H_2O$ from 2 mmol to 12 mmol, composites of 0.5Bi_2O_3/SnO_2, 1Bi_2O_3/SnO_2, 2Bi_2O_3/SnO_2 and 3Bi_2O_3/SnO_2 were obtained. Additionally, pure SnO_2 and Bi_2O_3 were prepared without addition of $Bi(NO_3)_3{\cdot}5H_2O$ or $Na_2SnO_3{\cdot}3H_2O$, respectively.

2.2. Evaluation of photocatalytic performance

A jacket photoreactor (Yaming Company, Shanghai) equipped with a 350 W Xenon lamp 15 cm from the center of the photoreaction tube was used in the photocatalytic experiment. Photocatalytic activities of the as-prepared samples were evaluated by photocatalytic degradation of BPA under simulated solar light. For each experimental run, 50 mg of each catalyst was added into 50 mL of 10 mg/L BPA solution, first stirred in the dark for 50 min to achieve an adsorption-desorption equilibrium between BPA molecules and catalyst particles and then exposed to light irradiation. During the photocatalytic process, 4 mL of the solution was taken out from the tube at regular time intervals and centrifuged to separate catalysts from the solution. The absorbance intensity of BPA was monitored by a UV–vis spectrophotometer (UV-1700, SHIMADU) with a 1 cm optical path quartz cuvette at the maximum absorption wavelength of 276 nm. Total organic carbon (TOC) values of BPA solutions were analyzed using a TOC analyzer (vario TOC, Germany). The concentration of BPA solution during the photocatalytic process was measured using an e2695 HPLC (Waters, USA) with a UV–Vis detector at 276 nm. The chromatographic separation was accomplished by a ZOR-BAX Eclipse Plus C18 column (5 μm, 4.6 × 150 mm), with fixed mobile phase of mixed water-methanol (3:7) at a flow rate of 1 mL/min. The oven temperature was maintained at 30 °C.

2.3. Characterization of the as-prepared materials

The crystal phases of the samples were analyzed by a Bruker-D8-AXS X-ray diffractometer system equipped with a Cu Kα radiation (k = 0.15406 nm) within the 2θ range from 10° to 80°. The morphologies and structures of the samples were observed using a Hitachi SU8010 field emission scanning electron microscope (FESEM) and JEM-2100 transmission electron microscopy (TEM). The elemental composition and chemical states of the samples were detected with an ESCALA 260Xi X-ray photoelectron spectroscopy (XPS). Light absorption characters of the materials were recorded using a Schimadzu UV-3600 Plus ultraviolet–visible diffuse reflectance spectrophotometer (UV–vis DRS) equipped with an integrating sphere at the wavelength range of 200–800 nm. Fourier transform-infrared spectra (FT-IR) were collected on a Spectrum 400 spectrometer in the range 400 to 4000 cm^{-1} using KBr as a reference. Photoluminescence (PL) spectra were performed on an Edinburgh Analytical Instrument FLS 980 Spectrophotometer at an excitation wavelength of 364 nm at room temperature. The specific surface areas of the samples were determined by N_2 sorption analysis using a MicrotracBEL Belsorp-max apparatus. Electron spin resonance (ESR) technique was used to determine the existence of oxygen species on Bruker A300 spectrometer.

2.4. Electrochemical measurement

Electrochemical measurements were conducted on a Zahner Zennium Electrochemical Workstation, in 0.1 mol/L Na_2SO_4 electrolyte solution using a standard three-electrode system, namely, saturated calomel electrode as reference electrode, platinum metal foil as counter electrode and indium tin oxide (ITO) conductive glass coated with the synthesized materials as working electrode. Photocurrent was measured with a 350 W Xenon lamp as the light source. Mott-Schottky test was carried out at the frequency of 1.0 kHz.

3. Results and discussion

3.1. Photocatalytic performance of Bi_2O_3/SnO_2 composites

Photocatalytic performances of the as-synthesized samples were evaluated by degrading BPA (10 mg/L) as a model pollutant (Fig. 1). Prior to the photocatalytic process, a dark adsorption experiment was performed to achieve an equilibrium adsorption state. Fig. 1a shows the process of BPA degradation in the presence of the different samples during 60 min of irradiation. The sample BO + SO in Fig. 1a denotes a mechanical mixture of Bi_2O_3 and SnO_2. It can be seen that the photocatalytic performance of the composite samples surpassed the control samples of pure Bi_2O_3, SnO_2, and BO + SO, illustrating the synergetic effect between Bi_2O_3 and SnO_2 and successful construction of Bi_2O_3/SnO_2 heterojunction photocatalyst. The photocatalytic performance of the composite samples first increase, then decrease with increasing the molar ratio of Bi_2O_3, with the optimal molar ratio at 1:1. The degradation rate of 1Bi_2O_3/SnO_2 at 60 min reached the highest value of 93.42%, while the degradation rates for pure Bi_2O_3 and SnO_2 at 60 min were 36.69% and 6.24%, respectively. The effective decomposition of BPA was also observed by recording the UV–vis absorption spectra (Fig. 1b) and HPLC spectra (Fig. 1c) of BPA degraded by 1Bi_2O_3/SnO_2 at different times during the degradation process. In Fig. 1b, the two absorption peaks at 224 and 276 nm, which were recognized as the characteristic absorption peak of BPA, decreased continuously with the reaction proceeding. At the end of the photocatalytic reaction, the peak intensity at 276 nm was close to the horizontal line. Analogously, the HPLC peak of BPA at 3.51 min decreased with the illumination time, which demonstrates the effective photodegradation of BPA by Bi_2O_3/SnO_2. TOC removal rates were analyzed to determine the

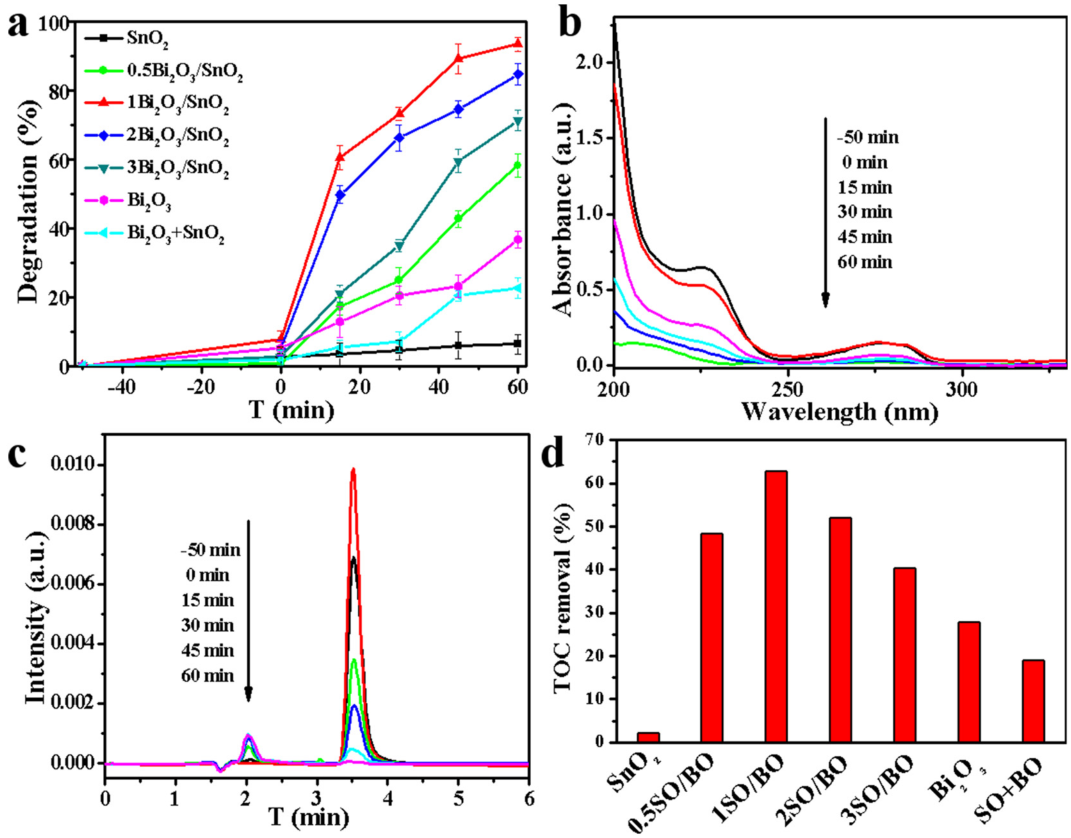

Fig. 1. Photocatalytic degradation efficiency of BPA solution with different samples (a); time-dependent UV–vis absorption spectra of BPA degraded by $1Bi_2O_3/SnO_2$ (b); time-dependent HPLC spectra of BPA degraded by $1Bi_2O_3/SnO_2$ (c); TOC removal efficiency of BPA solution with different samples (d) under simulated solar light illumination.

mineralization of BPA after photocatalytic degradation by different samples (Fig. 1d). The TOC removal rates of different samples showed a similar trend as the degradation rates, implying the effective mineralization of BPA by the photocatalysts. The highest TOC removal rate was 62.68% with $1Bi_2O_3/SnO_2$ after photocatalytic degradation for 60 min.

Fig. 2 shows the effect of different photocatalytic degradation conditions on the photocatalytic activity of $1Bi_2O_3/SnO_2$. The effect of the initial BPA concentration on the photocatalytic degradation efficiency of $1Bi_2O_3/SnO_2$ is shown in in Fig. 2a. It can be seen that the initial BPA concentration had an obvious impact on the photocatalytic degradation of BPA. Specifically, the lower initial BPA concentration, the faster degradation rate and higher degradation efficiency. The faster degradation rates were reflected in the shorter time required to reach the maximum degradation efficiencies (15 min, 45 min, 60 min and 75 min for the initial concentrations of 5 mg/L, 10 mg/L, 20 mg/L and 30 mg/L, respectively). This may be because of the relatively more active species for BPA molecules at the lower initial BPA concentration, so the decomposition speed was much faster. In addition, the degradation efficiencies of BPA at 75 min were 100%, 84.08%, 82.22%, 66.15%, 56.98% and 44.16% with the initial BPA concentration varying from 5 mg/L to 50 mg/L, respectively. The explanation for this phenomenon might be that the amount of active species generated under light irradiation was limited due to the fixed amount of catalyst. Therefore, as continuously enlarging the initial BPA concentration, the amount of active species became not enough to decompose the redundant BPA molecules [11]. Fig. 2b shows the influence of catalyst dosage on the photocatalytic degradation efficiency of BPA. As increasing the dosage of $1Bi_2O_3/SnO_2$ from 20 mg to 40 mg, the degradation efficiency of BPA at 75 min increased from 58.70% to 90.58, this may due to more active sites, as well as more active species created by the increased amount of catalyst. However, when continually increase the dosage of $1Bi_2O_3/SnO_2$ from 40 mg to 60 mg, the degradation efficiency of BPA had no significant increase, this phenomenon might attribute to the scattering and steric effect of light by the catalyst which was too much [27]. The effect of initial pH on the photocatalytic degradation of BPA by $1Bi_2O_3/SnO_2$ is shown in Fig. 2c. The degradation rates at acidic medium (91.74% at pH = 3.87, 78.51% at pH = 6.05) were higher than those at alkaline condition (61.98% at pH = 11.83, 46.28% at pH = 9.20). Under the acidic conditions, there are more hydrogen ions, which are positively charged and are likely to combine with negatively charged electrons produced under light irradiation and, as a result, the recombination of photo-induced electrons and holes was suppressed, leaving much holes to degrade BPA. Therefore, a suitable pH should be chosen for the treatment of wastewater containing BPA to achieve an ideal degradation efficiency.

Considering the practical usage of photocatalysts for the removal of various pollutants, the photocatalytic capability of $1Bi_2O_3/SnO_2$ composite is further investigated by the photocatalytic degradation of four antibiotics under sunlight irradiation (Fig. 2d), including sulfamethoxine (SMX), chloramphenicol (C), ciprofloxacin hydrochloride (CIP) and sulfonamide (SA). The degradation efficiencies of SMX, C, CIP, and SA at 100 min were 67.15%, 23.44%, 98.77% and 92.12%, respectively. The different photocatalytic performances of $1Bi_2O_3/SnO_2$ toward these antibiotic pollutants might be due to the different molecular structures of the pollutants, as well as the different adsorption activities between catalyst and the pollutant molecules. In summary, this Bi_2O_3/SnO_2 composite photocatalyst is efficient and can be expected to use in practical applications.

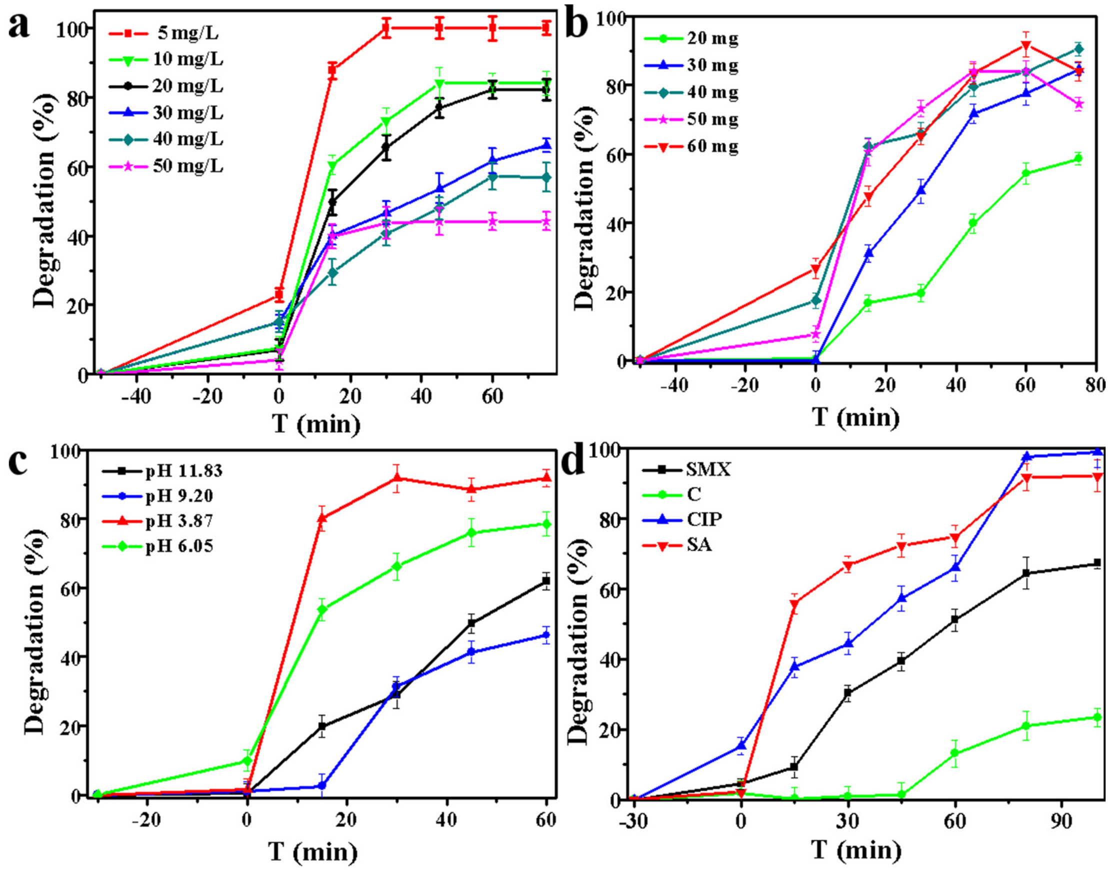

Fig. 2. Effect of BPA concentration on the degradation of BPA under the condition of $1Bi_2O_3/SnO_2$ mass = 50 mg and solution volume = 50 mL (a); effect of $1Bi_2O_3/SnO_2$ dosage on the degradation of BPA under the condition of BPA concentration = 10 mg/L and solution volume = 50 mL (b); effect of initial pH on the degradation of BPA under the condition of $1Bi_2O_3/SnO_2$ mass = 50 mg, BPA concentration = 10 mg/L and solution volume = 50 mL (c); effect of different pollutants on the photocatalytic activity of $1Bi_2O_3/SnO_2$ under the condition of $1Bi_2O_3/SnO_2$ mass = 50 mg, solution concentration = 10 mg/L, solution volume = 50 mL (d).

3.2. Characterization of the as-prepared materials

The crystal structure of the as-synthesized SnO_2, Bi_2O_3, and Bi_2O_3/SnO_2 composites was characterized by XRD (Fig. 3). XRD spectra of the pure Bi_2O_3 (JCPDS No.71-0465) exhibited strong diffraction peaks, indicating Bi_2O_3 was a typical crystalline material. The observed strong reflection peaks at 25.748°, 26.905°, 27.392°, 28.004°, 33.033°, 35.038°, 46.341°, and 55.457° were in good agreement with the (002), (−112), (−121), (012), (−122), (−212), (221), and (−224) crystal planes of monoclinic Bi_2O_3, respectively. For pure SnO_2, the characteristic diffraction peaks at 2θ = 26.611°, 33.893°, and 51.780° correspond with (110), (101), and (211) diffraction planes of the tetragonal phase SnO_2 (JCPDS No.41-1445) [28]. For the Bi_2O_3/SnO_2 composites, most of the diffraction peaks were assigned to Bi_2O_3 in the spectra, which was likely because the intensities of the SnO_2 peaks were quite weak and the peak positions overlapped with the Bi_2O_3 peaks. However, weak peaks located at 26.611° and 33.893° could be observed in the $0.5Bi_2O_3/SnO_2$ sample, which can be attributed to the (110) and (101) facets of SnO_2, which demonstrating that the Bi_2O_3/SnO_2 composites were successfully synthesized.

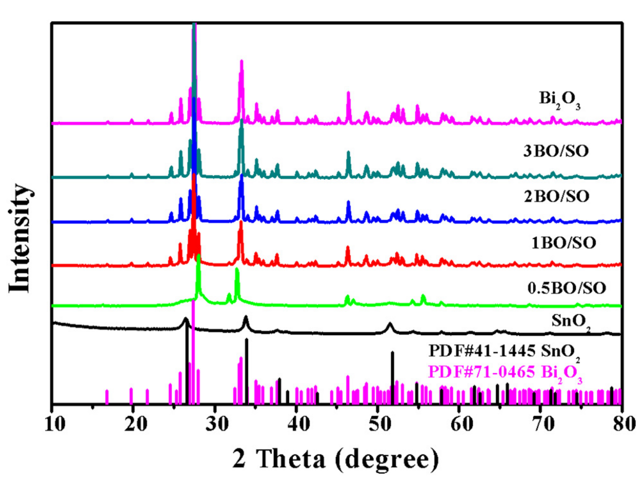

Fig. 3. XRD pattern of SnO_2, Bi_2O_3 and Bi_2O_3/SnO_2 composites.

To directly observe the morphologies and crystalline nature of pure SnO_2, Bi_2O_3, and Bi_2O_3/SnO_2 composites, SEM and TEM images were collected (Fig. 4). Fig. 4a shows that the pure SnO_2 exhibited a hollow sphere morphology with a rough surface, which had wall thickness from 0.58 to 0.84 μm, and the diameter of the hollow part from 0.61 to 0.97 μm. The morphology of pristine Bi_2O_3 (Fig. 4b) was composed of rods with branches, just like coral branches, with smooth surfaces and a trunk size of 1.41 μm × 0.35 μm and branch size from 0.25 μm to 0.56 μm × 0.23 μm. The morphology of the Bi_2O_3/SnO_2 composite (Fig. 4c) was similar to that of Bi_2O_3 and was composed of rods with branches. Moreover, the surface of the composite was covered with numerous nanoparticles that roughened the surface. The morphologies and structures of the Bi_2O_3/SnO_2 composites were further examined by TEM (Fig. 4d) and HRTEM (Fig. 2e). In Fig. 4d, nanoparticles can be seen dispersed over the surface of coral-like branches. The HRTEM image (Fig. 4e) provides a clearer observation of these two components. Two sets of different lattice images are observed at the interfaces, where

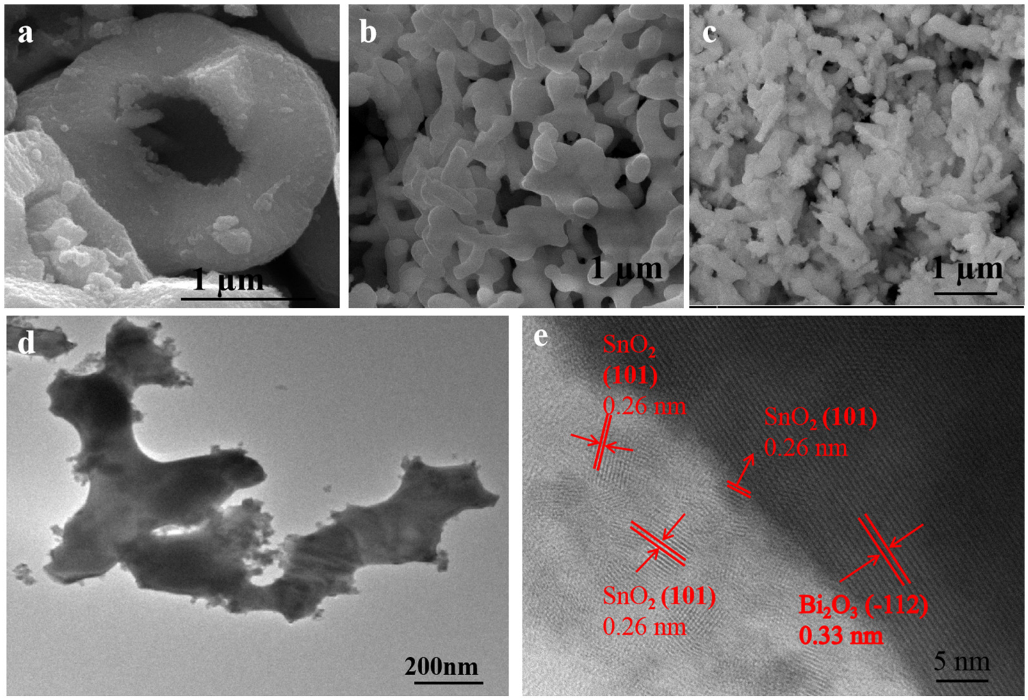

Fig. 4. SEM images of SnO_2 (a), Bi_2O_3 (b) and $1Bi_2O_3/SnO_2$ (c); low resolution TEM image of $1Bi_2O_3/SnO_2$ (d); high-resolution TEM image of $1Bi_2O_3/SnO_2$ (e).

the lattice fringes of 0.26 nm correspond to the (101) crystal facet of SnO_2 and the lattice fringe of 0.33 nm is consistent with the (−112) crystal facet of Bi_2O_3, respectively.

XPS was used to study the surface elemental composition and chemical states of as-prepared SnO_2, Bi_2O_3 and $1Bi_2O_3/SnO_2$ (Fig. 5). As shown in Fig. 5a, the Sn, O and Bi elements all existed in $1Bi_2O_3/SnO_2$ composite, revealing the successful coupling of Bi_2O_3 with SnO_2. The C 1s peak locating at 284.60 eV in the spectrum arose from the carbon-based contaminant. High-resolution XPS spectra of Bi4f, Sn3d and O1s are depicted in Fig. 5b–d. In Fig. 5b, the two XPS peaks located at

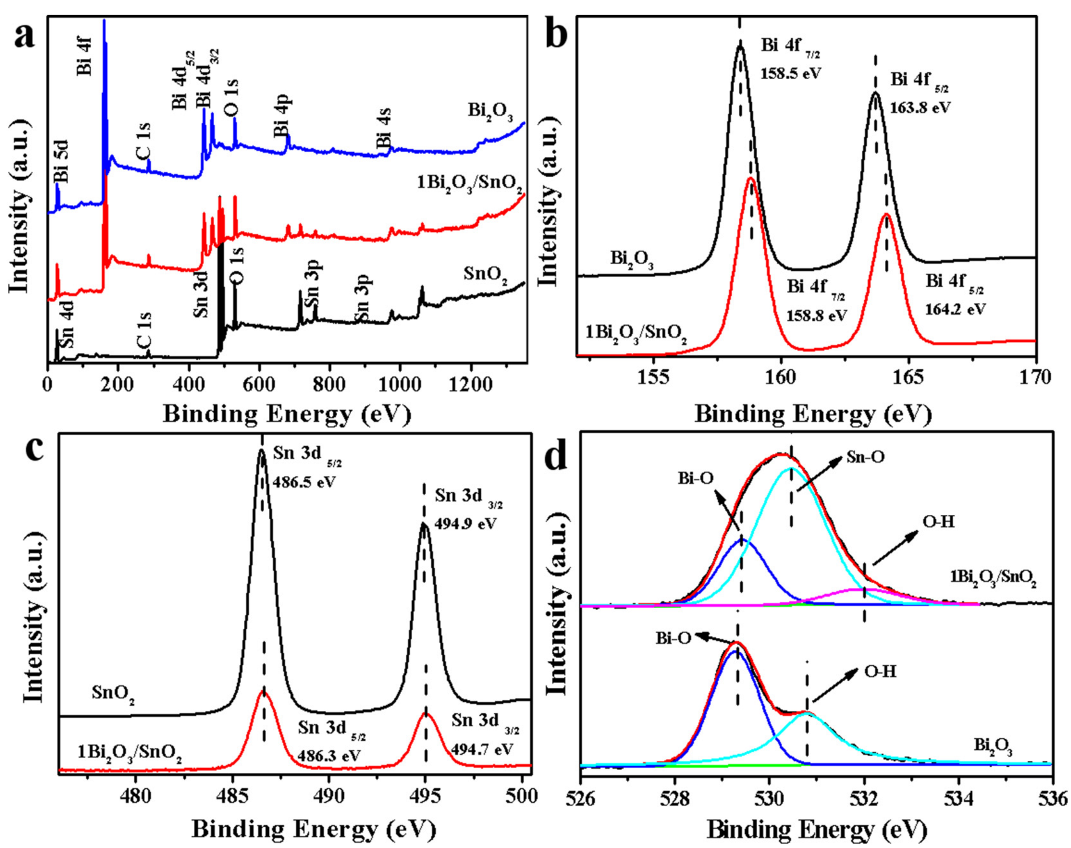

Fig. 5. Survey XPS spectra of SnO_2, Bi_2O_3 and $1Bi_2O_3/SnO_2$ (a) and high-resolution XPS spectra of Bi4f (b), Sn3d (c), and O1s (d).

binding energies of 158.50 eV and 163.80 eV were assigned to Bi $4f_{7/2}$ and Bi $4f_{5/2}$ of Bi^{3+} in pure Bi_2O_3 [29], respectively. After coupling with SnO_2, the binding energies of Bi $4f_{7/2}$ and Bi $4f_{5/2}$ shifted slightly to higher energy positions at 158.80 and 164.20 eV, respectively, which may be due to changes in the chemical environment caused by SnO_2 addition. Conversely, the peak positions of Sn $3d_{5/2}$ (486.30 eV) and Sn $3d_{3/2}$ (494.70 eV) in the $1Bi_2O_3/SnO_2$ composite were lower than those in pure SnO_2 (Sn $3d_{5/2}$ 486.50 eV and Sn $3d_{3/2}$ 494.90 eV), which is likely due to the higher electron density of $1Bi_2O_3/SnO_2$ (Fig. 5c) [30]. Fig. 5d illustrates the high-resolution XPS spectra of O1s for both Bi_2O_3 and $1Bi_2O_3/SnO_2$. The shoulder peak of O1s spectra indicates that multiple peak components can be obtained. By Gaussian fitting, O1s spectrum of Bi_2O_3 was split into two peaks and that of $1Bi_2O_3/SnO_2$ was split into three peaks. For Bi_2O_3, the two peaks located at 529.30 eV and 530.80 eV were assigned to Bi—O and O—H bonds, respectively. The split peaks of $1Bi_2O_3/SnO_2$ at binding energies of 529.45 eV, 530.45 eV and 532.00 eV correspond to Bi—O, Sn—O, and O—H bonds, respectively [18]. The higher binding energies of Bi—O and O—H bonds in $1Bi_2O_3/SnO_2$ compared with those in Bi_2O_3 demonstrated the strong interaction between the two components.

Fig. 6 shows the FT-IR spectra of pure SnO_2, Bi_2O_3, and Bi_2O_3/SnO_2 composite samples at 400–4000 cm^{-1}. Pure SnO_2 displays characteristic FT-IR peaks at 471.49, 1635.06, and 3180.17 cm^{-1}, which were assigned to stretching vibration of Sn—O, the bending vibrations, and the stretching vibrations of OH groups of absorbed molecular water, respectively [31]. Whereas, the FT-IR signals of Bi_2O_3 seem rather weak, the peaks located at 1388.36 and 1054.41 cm^{-1} correspond to the bonds of Bi—O in the BiO_3 unit and the BiO_4 unit, respectively [32]. In addition, two tiny peaks at 530.65 cm^{-1} were attributed to the stretching vibration of the Bi—O bands in Bi_2O_3 [31]. Notably, a new peak at 845.54 cm^{-1} belonging to Bi—O arose in the spectrum of Bi_2O_3/SnO_2 composites, which exists neither in the spectrum of Bi_2O_3 nor that of SnO_2. The newly formed bond reveals the strong interaction between the two components.

3.3. Possible mechanism of augmented photocatalytic activity

N_2 adsorption-desorption analysis was performed to determine the BET specific surface area and pore diameter distribution of SnO_2, Bi_2O_3, and $1Bi_2O_3/SnO_2$ samples (Fig. 7). The N_2 adsorption-desorption isotherms in Fig. 7a indicated all samples exhibited type IV isotherm according to the IUPAC classification, demonstrating the mesoporosity of the as-prepared samples. As depicted in the Barrett-Joyner-Halenda (BJH) pore size distribution curves in Fig. 7b, the average pore diameter of SnO_2 and $1Bi_2O_3/SnO_2$ were about 3.92 nm, which is in the mesoporous range. In contrast, the pore size distribution curves of Bi_2O_3 (inset in Fig. 7b) show peaks in both the mesoporous and the macroporous range. BET surface areas of the three samples were 13.916, 39.327, and 1.00546 $m^2 \cdot g^{-1}$ for SnO_2, $1Bi_2O_3/SnO_2$ and Bi_2O_3, respectively. Pore volumes of the three samples were 0.0281, 0.0605, and 0.0040 cm^3/g for SnO_2, $1Bi_2O_3/SnO_2$, and Bi_2O_3, separately. Generally, a high specific surface area and a large pore volume can provide more contact sites and larger accommodation space for the reactant molecule, and are thus beneficial to the enhancement of activity [33]. Therefore, enhanced photocatalytic performance could be achieved of $1Bi_2O_3/SnO_2$, which has the highest specific surface area and pore volume.

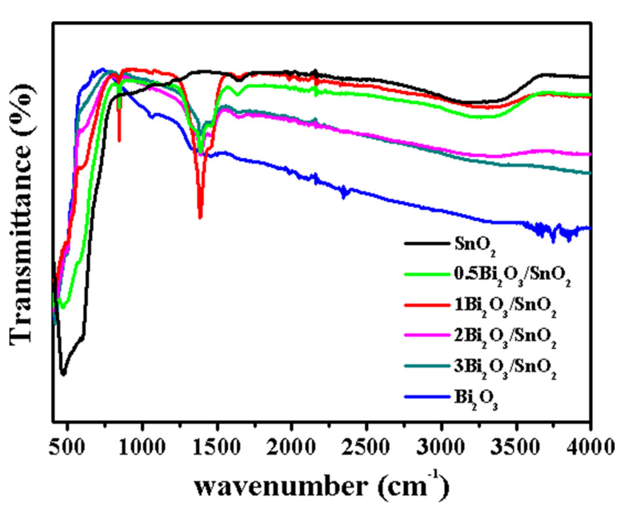

Fig. 6. FT-IR spectra of the as-prepared samples.

Light absorption property is an important factor that affects the photocatalytic activity of materials. The optical absorption properties of the as-prepared samples were investigated using the UV–vis diffuse reflectance spectra (Fig. 8a). The light absorption of pure SnO_2 lies in the UV region with an absorption edge at 369 nm, whereas pure Bi_2O_3 shows absorption from the UV to the visible light region with an absorption edge at 447 nm. The steep shapes of both the Bi_2O_3 and SnO_2 spectra indicate that the light absorption is due to the band-gap transition but not the transition from impurity levels [34]. As for the composite samples, red-shifts of the absorption edge and the enhancement of light absorption intensity take place compared with that of pure Bi_2O_3 and SnO_2, which might be attributed to the interaction between Bi_2O_3 and SnO_2. Need to say that $0.5Bi_2O_3/SnO_2$ had the strongest light absorption intensity and the biggest absorption edge (508 nm), however, it was not the one with the optimal activity. This is probably due to the existence of defects, which can be speculated from the two slopes rather than one steep slope of the DRS spectra of $0.5Bi_2O_3/SnO_2$. Additionally, the band gap energies (E_g) of Bi_2O_3, SnO_2, and $1Bi_2O_3/SnO_2$ were estimated from plots with $(Ah\nu)^2$ as the Y-axis and photon energy ($h\nu$) as the X-axis, where A, h and ν represent optical absorption coefficient, Planck constant, and photon frequency, respectively. The band gap of a material can be approximated from the intercept of the tangent to the X-axis. As shown in Fig. 8b, the E_g values of Bi_2O_3 and SnO_2 were estimated to be about 2.87 eV and 3.61 eV, respectively. While the E_g of $1Bi_2O_3/SnO_2$ (2.89 eV) is between that of Bi_2O_3 and SnO_2, which indicates that the interaction between Bi_2O_3 and SnO_2 is crucial to the intrinsic properties of Bi_2O_3/SnO_2 composite catalysts.

Photoluminescence spectroscopy was used to investigate the effect of Bi_2O_3 on the separation efficiency of electron-hole pairs of SnO_2. The PL spectra of pure SnO_2 (Fig. 9a) show a broad green emission peak at 551 nm. The intensity of the peak weakened following the order: SnO_2 > $0.5Bi_2O_3/SnO_2$ > Bi_2O_3 > $3Bi_2O_3/SnO_2$ > $2Bi_2O_3/SnO_2$ > $1Bi_2O_3/SnO_2$, which implies a higher photo-induced charge separation efficiency of SnO_2 after coupling with Bi_2O_3. As such, the higher photocatalytic performance of Bi_2O_3/SnO_2 composites was achieved. The highest PL peak of $0.5Bi_2O_3/SnO_2$ among the composite samples was probably related to the defects that acted as recombination centers in the sample. Therefore, the photocatalytic property of $0.5Bi_2O_3/SnO_2$ is not the best among the composites in spite of the good light absorption ability (Fig. 9a).

Transient photocurrents of the prepared catalysts were measured by turning the light on and off at 20 s intervals (Fig. 9b). The as-prepared samples had an obvious photoelectric response indicating from the periodic change in the currents. Although the value of the photocurrent differed from sample to sample, the Bi_2O_3/SnO_2 composites exhibited a higher photocurrent than pure SnO_2 and Bi_2O_3, implying the better separation efficiencies of photogenerated electron-hole pairs by Bi_2O_3/SnO_2 composites. With the increasing molar ratio of Bi_2O_3 in the composite, the photocurrent first increased and then decreased, the peak value was obtained with the $1Bi_2O_3/SnO_2$ sample.

Mott-Schottky tests were applied to determine the type of conductivity, as well as the flat band potentials of as-prepared products. As shown in Fig. 9c, the positive slopes of the linear part indicate the n-type feature of the materials. In addition, the flat band potentials that

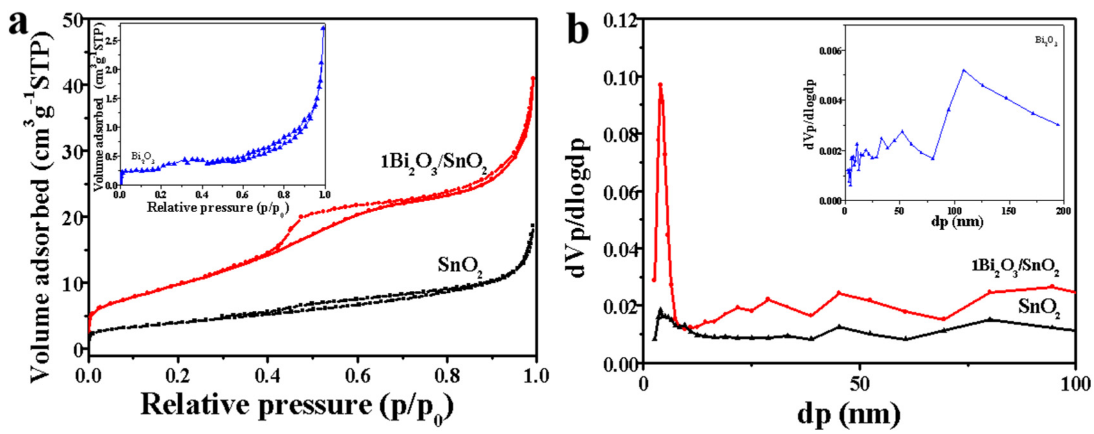

Fig. 7. N_2 adsorption/desorption isotherm (a) and pore size distribution of SnO_2, Bi_2O_3 and $1Bi_2O_3/SnO_2$ (b).

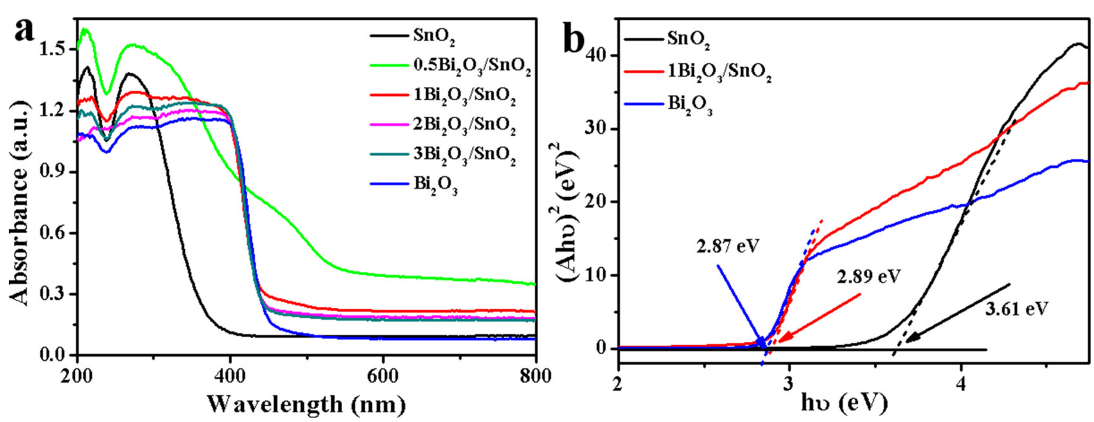

Fig. 8. UV–vis diffusion reflectance spectra of the as-prepared samples (a) and Tauc's plots of pure SnO_2, Bi_2O_3 and $1Bi_2O_3/SnO_2$ (b).

were obtained from the intercept of the tangent of the Mott-Schottky curves are −1.36, −0.54, and −0.60 V versus SCE for Bi_2O_3, SnO_2 and $1Bi_2O_3/SnO_2$, respectively, i.e., −1.12, −0.30, and −0.36 V versus normal hydrogen electrode (NHE) (NHE = SCE + 0.241 V) [35]. For n-type semiconductors, the flat band positions are thought to be approximately equal to that of the Fermi Levels (E_f) and the flat band potential is more positive by about 0.1 or 0.2 V than its conduction band potential (E_{CB}). Therefore, the conduction band potentials (E_{CB}) were calculated to be −1.32, −0.50, and −0.56 V versus NHE [36]. Accordingly, the valence band potentials of Bi_2O_3 and SnO_2 are 1.55 and 3.11 V, which were calculated from the equation of $E_{VB} = E_{CB} + E_g$.

ESR measurement was applied to determine the species produced in the photocatalytic degradation process. The DMPO-·OH adduct, DMPO-$\cdot O_2^-$ adduct and TEMP-$^1O_2$ adduct were tested both under dark and light irradiation (Fig. 10a–c). Obviously, signals of all the three adducts appeared only under light irradiation and no signal arose in the dark. The four peaks with an intensity ratio of 1:2:2:1 in Fig. 10a were ascribed to the DMPO-·OH adduct, while the two peaks with equal intensities in Fig. 10b and c were ascribed to DMPO-$\cdot O_2^-$ and TEMP-$^1O_2$ adduct, respectively. The ESR results indicate that ·OH, $\cdot O_2^-$ and $^1O_2$ were generated in the photocatalytic system. In order to probe the contribution of each specie to the photocatalytic degradation of BPA, the trapping experiment was carried out with isopropanol (IPA), ammonium oxalate (AO), methanol (MeOH), and sodium azide (SA) as quenchers to capture ·OH, h^+, $\cdot O_2^-$, and $^1O_2$, respectively. Moreover, a control experiment without adding any quenchers was also conducted for comparison. As shown in Fig. 10d, the addition of MeOH and IPA

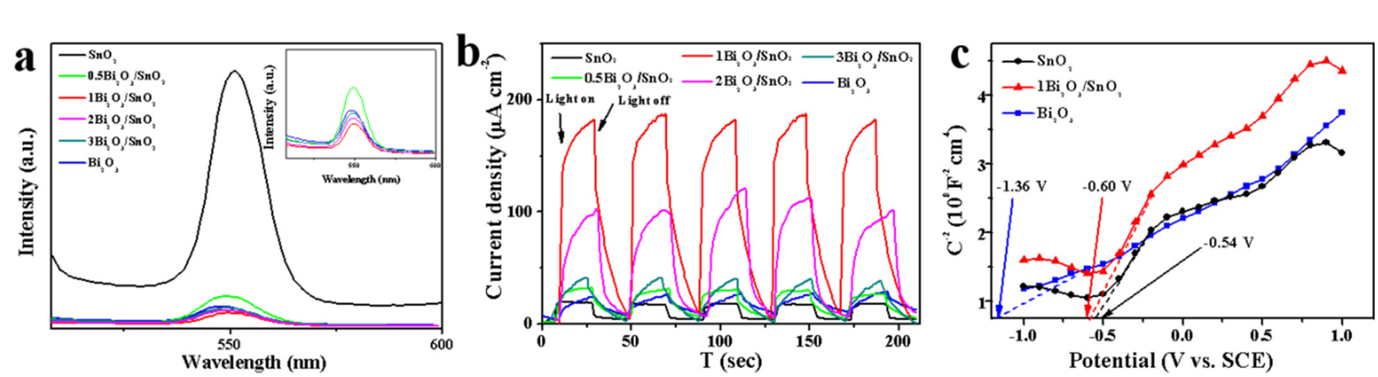

Fig. 9. Steady-state PL spectra of the as-prepared samples at an excitation wavelength of 364 nm (a); Photocurrent response of as-synthesized photocatalysts under irradiation of 350 W Xenon lamp (b); Mott-Schottky plots of Bi_2O_3, SnO_2 and $1Bi_2O_3/SnO_2$ at the frequency of 1.0 kHz (c).

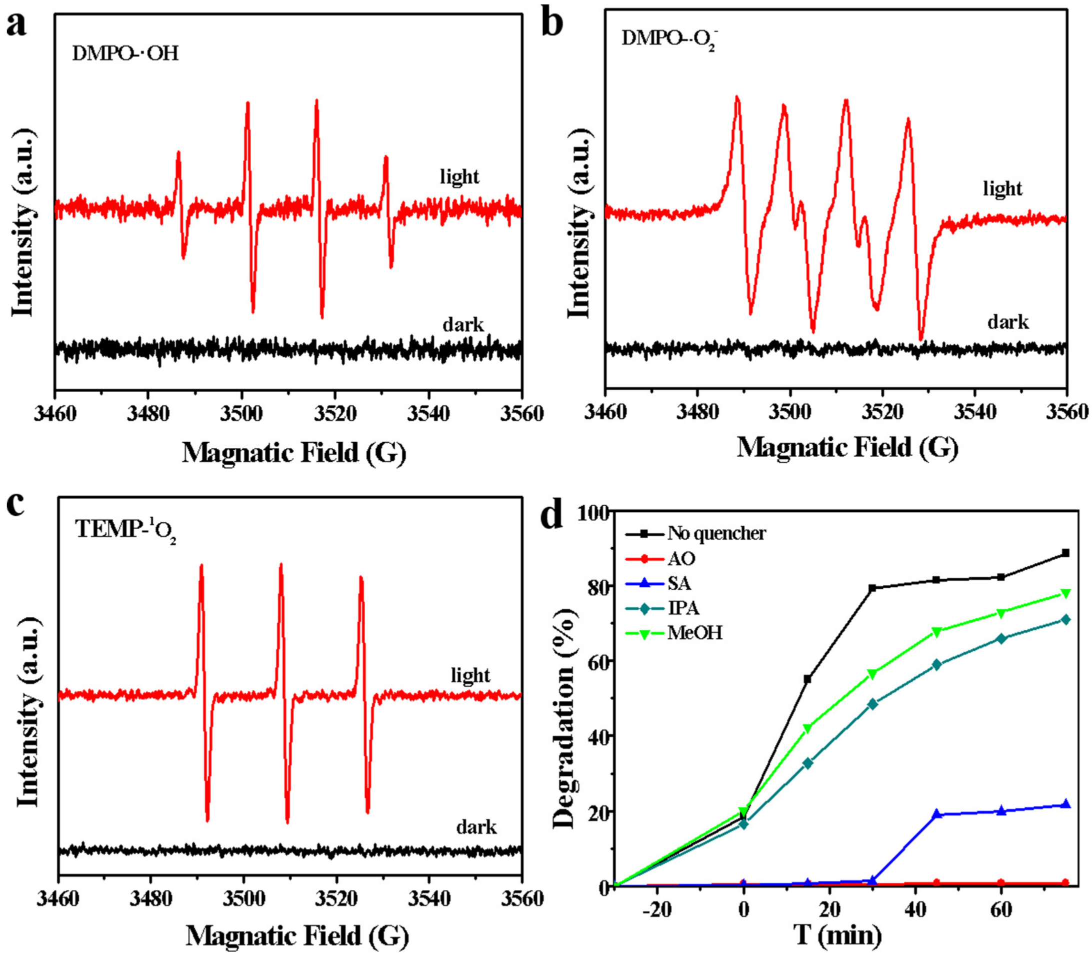

Fig. 10. ESR spectra of $1Bi_2O_3/SnO_2$ with or without light irradiation (a–c); photocatalytic decomposing of BPA by $1Bi_2O_3/SnO_2$ under simulated solar light with/without the quenchers (d).

had a slight influence on the photocatalytic degradation of BPA. However, degradation of BPA was greatly inhibited upon adding SA to the solution. What's more, degradation of BPA was completely suppressed when the quencher was AO. Above results indicated that $\cdot O_2^-$ and ·OH were not the critical reaction species in this photocatalytic system, while h^+ and $^1O_2$ played a crucial role in the photocatalytic process [37].

Based on the trapping experiment, ESR result and band position of the materials, a Z-scheme heterojunction was proposed for the photocatalytic mechanism of this composite photocatalyst, which was shown in the schematic illustration in Scheme 1. Under light irradiation, both Bi_2O_3 and SnO_2 can generate e^--h^+ pairs. Due to the electrostatic attraction between e^- and h^+ and closer distance from E_{CB} of SnO_2 to E_{VB} of Bi_2O_3, the e^- on E_{CB} of SnO_2 will combine with h^+ on E_{VB} of Bi_2O_3, leaving e^- on E_{CB} of Bi_2O_3 and h^+ on E_{VB} of SnO_2 to participate in the photocatalytic reaction. e^- on E_{CB} of Bi_2O_3 can reduce absorbed oxygen to $\cdot O_2^-$ due to the more negative E_{CB} of Bi_2O_3 (−1.32 V) than the potential of $O_2/\cdot O_2^-$ (−0.16 V). Meanwhile, h^+ on E_{VB} of SnO_2 can oxidize with OH^- or H_2O to produce ·OH because of the more positive E_{VB} of SnO_2 (+3.11 V) than the potential of $OH^-/\cdot OH$ (+1.99 V) and $H_2O/\cdot OH$ (+2.32 V). Moreover, $^1O_2$ can be generated via the reaction of $\cdot O_2^-$ with h^+ or energy transfer from excited state of $1Bi_2O_3/SnO_2$ to the ground state of absorbed oxygen molecule [38]. As above analysis, Z-scheme heterojunction as well as multiple active species, including h^+, $\cdot O_2^-$, ·OH and $^1O_2$ render the excellent photocatalytic performance of this composite catalysts.

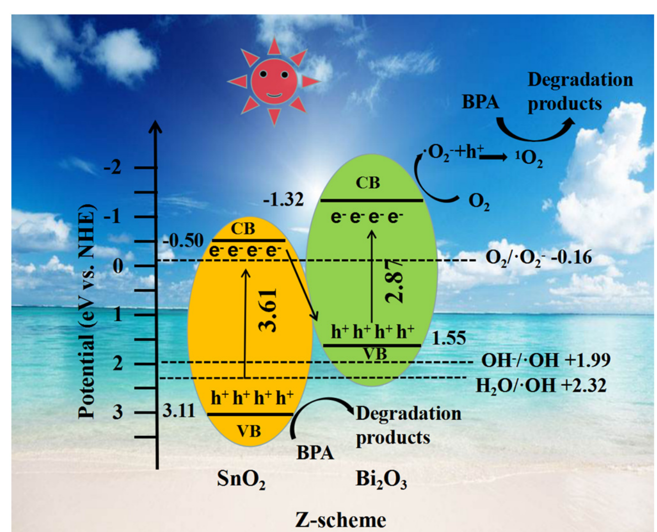

Scheme 1. Schematic illustration of photocatalytic process with Z-scheme Bi_2O_3/SnO_2 composite under sunlight irradiation.

4. Conclusions

In summary, Z-scheme Bi_2O_3/SnO_2 composites were successfully developed via a facile hydrothermal method. Such Z-scheme Bi_2O_3/SnO_2 composite (especially for $1Bi_2O_3/SnO_2$) exhibited augmented photocatalytic activity toward BPA under simulated solar light compared with the pure Bi_2O_3 and SnO_2 counterparts, which could be due to the enlargement of light absorption range, the enhanced specific surface area, and the reduced recombination rate of photo-induced electron-hole pairs. The photocatalytic conditions for BPA decomposing by $1Bi_2O_3/SnO_2$ were investigated, including initial BPA concentration, $1Bi_2O_3/SnO_2$ dosage, and initial pH of BPA aqueous solution. A suitable operating condition was selected as: 10 mg/L BPA, 40 mg $1Bi_2O_3/SnO_2$, and pH 3.87. Moreover, this composite catalyst also displayed broad-spectrum photocatalytic activity for effective degradation of the antibiotics SMX, C, CIP and SA. h^+, $\cdot O_2^-$, $\cdot OH$ and $^1O_2$ all existed in this photocatalytic system, yet h^+ and $^1O_2$ played the major role in the photocatalytic degrading BPA by Bi_2O_3/SnO_2 composite. Our study provides a rational strategy to fabricate Bi_2O_3/SnO_2 composites, which would be promising for practical applications for the efficient removal of various types of pollutants in environmental wastewater.

Declaration of competing interest

The authors have no conflicts of interest.

Acknowledgements

This work was supported by the NSFC (21677047, U1604137 and 51808199), the China Postdoctoral Science Foundation (2018M630825 and 2019T120624), Plan for University Scientific Innovation Talent of Henan Province (19HASTIT046), the Innovation Scientists and Technicians Troop Construction Projects of Henan Province, the Key Scientific Research Projects of Institutions of Higher Learning in Henan Province (18B530002). The authors also appreciate for the support from the Fund for Excellent Young Scholars (20180545) of Henan Normal University for the PhD.

Data availability

All the data required to reproduce these experiments are present in the article.

Appendix A. Supplementary data

Supplementary data to this article can be found online at https://doi.org/10.1016/j.matchar.2019.110036.

References

[1] P.A.K. Reddy, P.V.L. Reddy, E. Kwon, K.-H. Kim, T. Akter, S. Kalagara, Recent advances in photocatalytic treatment of pollutants in aqueous media, Environ. Int. 91 (2016) 94–103.
[2] M. Rani, U. Shanker, Insight in to the degradation of bisphenol A by doped ZnO@ZnHCF nanocubes: high photocatalytic performance, J. Colloid. Interf. Sci. 530 (2018) 16–28.
[3] Y. Zhou, G. Cheng, K. Chen, J. Lu, J. Lei, S. Pu, Adsorptive removal of bisphenol A, chloroxylenol, and carbamazepine from water using a novel beta-cyclodextrin polymer, Ecotoxicol. Environ. Saf. 170 (2019) 278–285.
[4] X. Zhang, Y. Ding, H. Tang, X. Han, L. Zhu, N. Wang, Degradation of bisphenol A by hydrogen peroxide activated with $CuFeO_2$ microparticles as a heterogeneous Fenton-like catalyst: efficiency, stability and mechanism, Chem. Eng. J. 236 (2014) 251–262.
[5] J. Sharma, I.M. Mishra, D.D. Dionysiou, V. Kumar, Oxidative removal of Bisphenol A by UV-C/peroxymonosulfate (PMS): kinetics, influence of co-existing chemicals and degradation pathway, Chem. Eng. J. 276 (2015) 193–204.
[6] M. Dükkancı, Sono-photo-Fenton oxidation of bisphenol-A over a $LaFeO_3$ perovskite catalyst, Ultrason. Sonochem. 40 (2018) 110–116.
[7] J. Sharma, I.M. Mishra, V. Kumar, Degradation and mineralization of Bisphenol A (BPA) in aqueous solution using advanced oxidation processes: UV/H_2O_2 and $UV/S_2O_8^{2-}$ oxidation systems, J. Environ. Manag. 156 (2015) 266–275.
[8] B. Chen, L. Zhou, Y. Tian, J. Yu, J. Lei, L. Wang, Y. Liu, J. Zhang, Z-scheme inverse opal CN/BiOBr photocatalysts for highly efficient degradation of antibiotics, Phys. Chem. Chem. Phys. 21 (2019) 12818–12825.
[9] S. Dong, J. Feng, Y. Li, L. Hu, M. Liu, Y. Wang, Y. Pi, J. Sun, J. Sun, Shape-controlled synthesis of $BiVO_4$ hierarchical structures with unique natural-sunlight-driven photocatalytic activity, Appl. Catal. B-Environ. 152-153 (2014) 413–424.
[10] S.Y. Dong, L.F. Cui, Y.L. Zhao, Y.W. Wu, L.J. Xia, X.F. Su, C.Y. Zhang, D. Wang, W. Guo, J.H. Sun, Crystal structure and photocatalytic properties of perovskite $MSn(OH)_6$ (M = Cu and Zn) composites with d^{10}-d^{10} configuration, Appl. Surf. Sci. 463 (2019) 659–667.
[11] L.Y. Yang, S.Y. Dong, J.H. Sun, J.L. Feng, Q.H. Wu, S.P. Sun, Microwave-assisted preparation, characterization and photocatalytic properties of a dumbbell-shaped ZnO photocatalyst, J. Hazard. Mater. 179 (2010) 438–443.
[12] L. Tan, C. Yu, M. Wang, S. Zhang, J. Sun, S. Dong, J. Sun, Synergistic effect of adsorption and photocatalysis of 3D $g\text{-}C_3N_4$-agar hybrid aerogels, Appl. Surf. Sci. 467–468 (2019) 286–292.
[13] W. Luo, X. Chen, Z. Wei, D. Liu, W. Yao, Y. Zhu, Three-dimensional network structure assembled by $g\text{-}C_3N_4$ nanorods for improving visible-light photocatalytic performance, Appl. Catal. B Environ. 255 (2019) 117761.
[14] W. Wei, Y. Zhu, TiO_2 @perylene diimide full-spectrum photocatalysts via semi-core-shell structure, Small (2019) 1903933–1903940.
[15] Y. Sheng, Z. Wei, H. Miao, W. Yao, H. Li, Y. Zhu, Enhanced organic pollutant photodegradation via adsorption/photocatalysis synergy using a 3D $g\text{-}C_3N_4/TiO_2$ free-separation photocatalyst, Chem. Eng. J. 370 (2019) 287–294.
[16] Y. Liu, Y. Jiao, Z. Zhang, F. Qu, A. Umar, X. Wu, Hierarchical SnO_2 nanostructures made of intermingled ultrathin nanosheets for environmental remediation, smart gas sensor, and supercapacitor applications, Acs. Appl. Mater. Inter. 6 (2014) 2174–2184.
[17] J. Wang, J. Jin, X. Wang, S. Yang, Y. Zhao, Y. Wu, S. Dong, J. Sun, J. Sun, Facile fabrication of novel $BiVO_4/Bi_2S_3/MoS_2$ n-p heterojunction with enhanced photocatalytic activities towards pollutant degradation under natural sunlight, J. Colloid Interface Sci. 505 (2017) 805–815.
[18] H. Liu, C. Du, M. Li, S. Zhang, H. Bai, L. Yang, S. Zhang, One-pot hydrothermal synthesis of SnO_2/BiOBr heterojunction photocatalysts for the efficient degradation of organic pollutants under visible light, Acs. Appl. Mater. Inter. 10 (2018) 28686–28694.
[19] A. Nouri, A. Fakhri, Synthesis, characterization and photocatalytic applications of N-, S-, and C-doped SnO_2 nanoparticles under ultraviolet (UV) light illumination, Spectrochim. Acta, Part A. 138 (2015) 563–568.
[20] J.S. Kim, Y.B. Kim, S.K. Baek, Y.D. Yun, S.H. Jung, S.W. Cho, C.H. Ahn, H.K. Cho, Compositionally graded SnO_2/TiO_2 bi-layered compounds with dramatically enhanced charge transport efficiency for self-driven water purification applications, J. Alloys Compd. 776 (2019) 839–849.
[21] M.M. Khan, S.A. Ansari, M.E. Khan, M.O. Ansari, B.-K. Min, M.H. Cho, Visible light-induced enhanced photoelectrochemical and photocatalytic studies of gold decorated SnO_2 nanostructures, New J. Chem. 39 (2015) 2758–2766.
[22] J. Li, Y. Chen, Q. Wu, J. Wu, Y. Xu, Synthesis of sea-urchin-like Fe_3O_4/SnO_2 heterostructures and its application for environmental remediation by removal of p-chlorophenol, J. Mater. Sci. 54 (2018) 1341–1350.
[23] M.T. Uddin, Y. Nicolas, C. Olivier, T. Toupance, L. Servant, M.M. Muller, H.J. Kleebe, J. Ziegler, W. Jaegermann, Nanostructured SnO_2-ZnO heterojunction photocatalysts showing enhanced photocatalytic activity for the degradation of organic dyes, Inorg. Chem. 51 (2012) 7764–7773.
[24] R. Yin, Q. Luo, D. Wang, H. Sun, Y. Li, X. Li, J. An, $SnO_2/g\text{-}C_3N_4$ photocatalyst with enhanced visible-light photocatalytic activity, J. Mater. Sci. 49 (2014) 6067–6073.
[25] N. Sun, Y. Qu, S. Chen, R. Yan, M. Humayun, Y. Liu, L. Bai, L. Jing, H. Fu, Efficient photodecomposition of 2,4-dichlorophenol on recyclable phase-mixed hierarchically structured Bi_2O_3 coupled with phosphate-bridged nano-SnO_2, Environ. Sci-Nano. 4 (2017) 1147–1154.
[26] T. Qiu, S. Liu, H. Cai, Y. Zhou, K. Chen, Y. Huang, Q. Feng, One step solid-state reaction synthesis, characterization, and catalytic performance of n–p SnO_2/Bi_2O_3 composite, J. Mater. Sci. - Mater. Electron. 29 (2018) 17463–17472.
[27] C. Yu, P. Yang, L. Tie, S. Yang, S. Dong, J. Sun, J. Sun, One-pot fabrication of β-$Bi_2O_3@Bi_2S_3$ hierarchical hollow spheres with advanced sunlight photocatalytic RhB oxidation and Cr(VI) reduction activities, Appl. Surf. Sci. 455 (2018) 8–17.
[28] R. Mani, K. Vivekanandan, N.P. Subiramaniyam, Photocatalytic activity of different organic dyes by using pure and Fe doped SnO_2 nanopowders catalyst under UV light irradiation, J. Mater. Sci. - Mater. Electron. 28 (2017) 13846–13852.
[29] C.F. Yu, K. Wang, P.Y. Yang, S.N. Yang, C. Lu, Y.Z. Song, S.Y. Dong, J.Y. Sun, J.H. Sun, One-pot facile synthesis of $Bi_2S_3/SnS_2/Bi_2O_3$ ternary heterojunction as advanced double Z-scheme photocatalytic system for efficient dye removal under sunlight irradiation, Appl. Surf. Sci. 420 (2017) 233–242.
[30] Y. Wang, J. Zhao, Z. Chen, F. Zhang, W. Guo, H. Lin, F. Qu, Construction of Z-scheme $MoSe_2$/CdSe hollow nanostructure with enhanced full spectrum photocatalytic activity, Appl. Catal. B-Environ. 244 (2019) 76–86.
[31] J. Li, T. Peng, Y. Zhang, C. Zhou, A. Zhu, Polyaniline modified SnO_2 nanoparticles for efficient photocatalytic reduction of aqueous Cr(VI) under visible light, Sep. Purif. Technol. 201 (2018) 120–129.
[32] H. Tang, W. Yang, L. Fu, J. Zhu, D. Li, L. Zhou, Excellent adsorption capacity and photocatalytic regeneration of nanoparticles-assembled mesoporous Cu_2O/Bi_2O_3 composites for removal of methyl orange, Mater. Res. Express. 6 (2019) 085532.
[33] B. Babu, A.N. Kadam, R.V.S.S.N. Ravikumar, C. Byon, Enhanced visible light photocatalytic activity of Cu-doped SnO_2 quantum dots by solution combustion synthesis, J. Alloys Compd. 703 (2017) 330–336.
[34] S. Dong, C. Yu, Y. Li, Y. Li, J. Sun, X. Geng, Controlled synthesis of T-shaped $BiVO_4$ and enhanced visible light responsive photocatalytic activity, J. Solid State Chem. 211 (2014) 176–183.
[35] Y. Luo, B. Deng, Y. Pu, A. Liu, J. Wang, K. Ma, F. Gao, B. Gao, W. Zou, L. Dong, Interfacial coupling effects in $g\text{-}C_3N_4/SrTiO_3$ nanocomposites with enhanced H_2 evolution under visible light irradiation, Appl. Catal. B-Environ. 247 (2019) 1–9.
[36] Y. Zhao, Y. Wang, X. Liang, H. Shi, C. Wang, J. Fan, X. Hu, E. Liu, Enhanced photocatalytic activity of Ag-$CsPbBr_3$/CN composite for broad spectrum

photocatalytic degradation of cephalosporin antibiotics 7-ACA, Appl. Catal. B-Environ. 247 (2019) 57–69.

[37] L. Tie, C. Yu, Y. Zhao, H. Chen, S. Yang, J. Sun, S. Dong, J. Sun, Fabrication of WO_3 nanorods on reduced graphene oxide sheets with augmented visible light photocatalytic activity for efficient mineralization of dye, J. Alloys Compd. 769 (2018) 83–91.

[38] G. Ba, Z. Liang, H. Li, N. Du, J. Liu, W. Hou, Simultaneous formation of mesopores and homojunctions in graphite carbon nitride with enhanced optical absorption, charge separation and photocatalytic hydrogen evolution, Appl. Catal. B-Environ. 253 (2019) 359–368.